J. Fluid Mech. (1999), *vol.* 399, *pp.* 251–275. Printed in the United Kingdom

Bénard–Marangoni convection at low Prandtl number

By THOMAS BOECK AND ANDRÉ THESS

Department of Mechanical Engineering, Ilmenau University of Technology, PO Box 100565, 98684 Ilmenau, Germany

(Received 5 February 1999 and in revised form 25 June 1999)

Surface-tension-driven Bénard convection in low-Prandtl-number fluids is studied by means of direct numerical simulation. The flow is computed in a three-dimensional rectangular domain with periodic boundary conditions in both horizontal directions and either a free-slip or no-slip bottom wall using a pseudospectral Fourier–Chebyshev discretization. Deformations of the free surface are neglected. The smallest possible domain compatible with the hexagonal flow structure at the linear stability threshold is selected. As the Marangoni number is increased from the critical value for instability of the quiescent state to approximately twice this value, the initially stationary hexagonal convection pattern becomes quickly time-dependent and eventually reaches a state of spatio-temporal chaos. No qualitative difference is observed between the zero-Prandtl-number limit and a finite Prandtl number corresponding to liquid sodium. This indicates that the zero-Prandtl-number limit provides a reasonable approximation for the prediction of low-Prandtl-number convection. For a free-slip bottom wall, the flow always remains three-dimensional. For the no-slip wall, two-dimensional solutions are observed in some interval of Marangoni numbers. Beyond the Marangoni number for onset of inertial convection in two-dimensional simulations, the convective flow becomes strongly intermittent because of the interplay of the flywheel effect and three-dimensional instabilities of the two-dimensional rolls. The velocity field in this intermittent regime is characterized by the occurrence of very small vortices at the free surface which form as a result of vortex stretching processes. Similar structures were found with the free-slip bottom at slightly smaller Marangoni number. These observations demonstrate that a high numerical resolution is necessary even at moderate Marangoni numbers in order to properly capture the small-scale dynamics of Marangoni convection at low Prandtl numbers.

1. Introduction

Surface-tension-driven Bénard convection, which occurs in a plane fluid layer with an upper free surface heated from below, can serve as a prototype system for other surface-tension-driven flows due to the conceptual simplicity of the setup. The understanding of this type of convection (usually referred to as Bénard–Marangoni convection and abbreviated as BMC) therefore presents one of the fundamental problems in fluid mechanics. Although it is still less well studied than its buoyancy-driven counterpart (Rayleigh–Bénard convection or RBC for short), it has received considerable attention over the last few years. The majority of both experimental and theoretical works on BMC deals with fluids with high Prandtl number from the viewpoint of pattern formation in dissipative systems, e.g. Bestehorn 1993; Golovin,

Nepomnyashchy & Pismen 1997; Van Hook *et al.* 1997; Eckert, Bestehorn & Thess 1998. Typically, such flows have small Reynolds number and are either stationary or are only weakly time-dependent.

Marangoni convection in low-Prandtl-number fluids, i.e. liquid metals or semiconductor melts, plays an important role in industrial processes such as crystal growth (Davis 1987) or electron beam evaporation (Schiller, Heisig & Panzer 1982; Pumir & Blumenfeld 1996). Due to the strong thermal forcing and the low kinematic viscosity of liquid metals these flows usually have high Reynolds numbers, i.e. they are usually time-dependent or even turbulent. In addition, liquid metals are not transparent and are difficult to handle experimentally. For these reasons, numerical simulations are often used for investigations of low-Prandtl-number convection. The geometries in the numerical studies frequently resemble actual experimental or industrial setups such as the floating zone (Kuhlmann & Rath 1993; Levenstam & Amberg 1995; Zebib, Homsy & Meiburg 1985; Carpenter & Homsy 1990). Because of this technological background it is perhaps not very surprising that there are only few works about BMC at low Prandtl number. Among them are the study of Ginde, Gill & Verhoeven (1989), which is the only experimental one to our knowledge, the theoretical studies of Dauby *et al.* (1993) and of Thess & Bestehorn (1995) which predict the occurrence of 'inverted' hexagons at the onset of convection for sufficiently small Prandtl numbers, and the previous direct numerical simulations of the authors (Boeck & Thess 1997, 1998) of the two-dimensional case. The present paper extends these previous numerical investigations to three spatial dimensions. We have systematically studied the flows emerging upon increasing the heating. The observed phenomena include steady cellular convection as well as convection with regular and chaotic time-dependence. In many respects, our approach parallels the work by Thual (1992) on RBC at low or even zero Prandtl number. The computational domain we use is about twice the size of the geometries studied by Thual.

The main focus of the present paper will be on the question of regularity of the zero-Prandtl-number limit. For RBC as well as for BMC it turns out that the limit of zero Prandtl number becomes meaningless for two-dimensional rolls when the applied temperature gradient (measured by the dimensionless Rayleigh/Marangoni number) exceeds a certain critical value. The so-called flywheel effect then leads to an unbounded exponential growth of the flow amplitude with time. This effect occurs because the nonlinear terms in the Navier–Stokes equations can be balanced by pressure gradients for two-dimensional rolls in an integral sense, and the nonlinearity in the energy equation disappears in the limit of zero Prandtl number (Proctor 1977; Busse & Clever 1981). According to Thual (1992), the flywheel effect was apparently first noted by Herring in 1970 for RBC. The authors have recently found it in BMC (Boeck & Thess 1997). For finite Prandtl numbers the amplitude of the two-dimensional flow remains finite, but the relevant scale of velocity and temperature is the much larger thermal scale rather than the viscous scale (see § 4.2 for details). The associated mode of convection is called inertial convection. It indicates that the zero-Prandtl-number limit is singular in the way described above.

The existence of inertial convection in three-dimensional RBC still appears to be a controversial issue. Chiffaudel, Fauve & Perrin (1987) have reported experimental observations which support its existence, but numerical studies are either inconclusive or contradict this view (Clever & Busse 1990; Thual 1992). For BMC, nothing is known in the three-dimensional case since the simulations reported in Thess & Bestehorn (1995) did not reach the Marangoni number required for inertial convection. In the present paper we shall present numerical simulations for Marangoni numbers

ranging from the onset of convection up to values beyond the onset of the flywheel effect or inertial convection as observed in two dimensions. In this way, the question of existence of inertial convection in three-dimensional BMC can be addressed for the first time. We have also attempted to obtain a detailed overview of the flow patterns up to the onset of chaotic convection. Two different Prandtl numbers are considered, namely a finite Prandtl number approximately equal to that of liquid sodium and the limit of zero Prandtl number.

The paper is organized as follows. In the following section we will briefly list the basic equations and discuss the limit of zero Prandtl number. We continue with the description of the numerical scheme in § 3. Results for the case of free-slip boundary conditions at the bottom of the fluid layer will be presented in § 4. After that, the no-slip condition is considered. Finally, we shall present our conclusions and indicate directions for future work.

2. Basic equations

We consider a planar fluid layer of thickness d with a free upper surface, which is heated from below. Our theoretical model involves the basic assumptions of zero buoyancy force and a non-deflecting upper surface. Only surface tension forces drive the convective flow. This assumption is valid when the layer is sufficiently thin or under microgravity conditions.

The basic equations will be formulated in a Cartesian coordinate system, where the isothermal bottom of the layer coincides with the plane $z = 0$. Periodic boundary conditions apply in the x- and y-directions. The thickness d is chosen as lengthscale for non-dimensionalization, i.e. the free surface is located at $z = 1$. The dimensionless quantities L_x and L_y denote the periodicity length with respect to x and y.

The fluid in the layer is an incompressible Newtonian liquid satisfying the Navier–Stokes equation together with the continuity and the heat equations. At the bottom of the layer we assume either free-slip or no-slip conditions. The heat flux density at the free surface $z = 1$ is modelled by Newton's law of cooling

$$-\frac{\lambda}{d}\frac{\partial T}{\partial z} = -\alpha\,(T_* - T_s(x, y))\,, \tag{2.1}$$

where $T_s = T(x, y, 1)$ denotes the surface temperature of the fluid and T_* stands for the (constant) ambient temperature. The remaining quantities λ and α are the heat conductivity and the heat transfer coefficient. In the conductive state the vertical temperature profile is linear. The temperature difference across the layer is then given by

$$\Delta T_0 = T_b - T_s = \frac{Bi}{1 + Bi}(T_b - T_*), \qquad Bi = \frac{\alpha d}{\lambda}, \tag{2.2}$$

with T_b as bottom temperature and the Biot number Bi as a non-dimensional parameter. It is convenient to consider the deviation θ from the the conductive profile defined by

$$T = \theta + T_b - \Delta T_0 z. \tag{2.3}$$

Notice that $\theta(x, y, z) \leqslant \Delta T_0 z$ since the fluid cannot become hotter than the bottom wall, and that z is a non-dimensional quantity in the above equation, whereas the temperatures are still dimensional. Throughout this paper, we shall exclusively deal with the limit of zero Biot number. It corresponds to a constant heat flux density at

the free surface. Notice that $Bi(T_b - T_*)$ has to remain finite as $Bi \to 0$ in order to maintain a temperature gradient in the layer.

The force balance at the free surface requires that

$$\rho\nu \frac{\partial \boldsymbol{v}}{\partial z} = \nabla\sigma, \tag{2.4}$$

where $\boldsymbol{v}$ is the velocity, σ denotes the surface tension, ρ the fluid density and ν the kinematic viscosity (Landau & Lifshitz 1987). The surface tension decreases linearly with temperature as

$$\sigma = \sigma(T_r) - \gamma(T - T_r), \tag{2.5}$$

where T_r stands for a reference temperature.

The equations will be given in a form based on viscous velocity scaling, i.e. we take v/d as velocity scale and d^2/ν as time scale. Furthermore, we choose $\nu\Delta T_0/\kappa$ as the scale of θ, where κ denotes the thermal diffusivity of the fluid. The dimensionless equations and boundary conditions in the case of zero Biot number read

$$\frac{\partial \boldsymbol{v}}{\partial t} + (\boldsymbol{v}\cdot\nabla)\boldsymbol{v} = -\nabla p + \nabla^2\boldsymbol{v}, \tag{2.6}$$

$$\nabla\cdot\boldsymbol{v} = 0, \tag{2.7}$$

$$P\left\{\frac{\partial\theta}{\partial t} + (\boldsymbol{v}\cdot\nabla)\theta\right\} = \nabla^2\theta + v_z, \tag{2.8}$$

$$\frac{\partial v_x}{\partial z} + Ma\,\frac{\partial\theta}{\partial x} = \frac{\partial v_y}{\partial z} + Ma\,\frac{\partial\theta}{\partial y} = v_z = \frac{\partial\theta}{\partial z} = 0 \quad \text{at } z = 1, \tag{2.9}$$

$$\frac{\partial v_x}{\partial z} = \frac{\partial v_y}{\partial z} = v_z = \theta = 0 \quad \text{at } z = 0 \quad \text{(free-slip)}, \tag{2.10}$$

$$v_x = v_y = v_z = \theta = 0 \quad \text{at } z = 0 \quad \text{(no-slip)}, \tag{2.11}$$

with the Marangoni number

$$Ma = \frac{\gamma\Delta T_0 d}{\rho\nu\kappa} \tag{2.12}$$

as control parameter. The other parameter $P = \nu/\kappa$ denotes the Prandtl number. The scale for θ has been chosen in such a way that a coupling of velocity and temperature is maintained also in the limit $P = 0$, i.e. when the left-hand side of (2.8) vanishes. This limit will be referred to as the (viscous) zero-Prandtl-number limit. The advantage of this limit for the numerical computations consists in the saving of four Fourier transforms per time step, which reduces the amount of computation by about 30% (9 vs. 13 transforms).

We also remark that the same limit has been considered in the work of Thual (1992) for RBC. Other limiting cases based on different temperature and velocity scalings are also discussed in that work, and it is argued that these other cases either model transients or flows where thermal convection is merely a side effect.

Convective heat transport is measured by the non-dimensional Nusselt number Nu defined as the ratio between the total heat flux and the conductive heat flux. In contrast to convection between isothermal plates with fixed temperatures, convection reduces the temperature drop across the layer. Since the contribution of heat conduction to the total heat transport is thereby reduced, we have to compute the conductive heat

flux for the present, reduced surface temperature. The result reads

$$Nu = \frac{1}{1 - P\langle\theta_s\rangle}, \tag{2.13}$$

where

$$\langle\theta_s\rangle = \frac{1}{L_x L_y}\int_0^{L_x}\int_0^{L_y}\theta(x, y, 1)\,\mathrm{d}x\,\mathrm{d}y \tag{2.14}$$

denotes the mean perturbation of the surface temperature.

In the zero-Prandtl-number limit Nu equals unity. We can determine Nu for $P > 0$ from this limit if we regard the solution of the zero-Prandtl-number equations as the leading term in an expansion in P. The calculations are given in Boeck & Thess (1997). We only list the final results. The mean surface temperature perturbation $\langle\theta_s\rangle$ and $Nu - 1$ read

$$\langle\theta_s\rangle = P\int_0^1\langle v_z\theta\rangle\,\mathrm{d}z + O(P^2), \tag{2.15}$$

$$Nu - 1 = P^2\int_0^1\langle v_z\theta\rangle\,\mathrm{d}z + O(P^3), \tag{2.16}$$

where v_z and θ are the solutions of the zero-Prandtl-number equations. Due to its connection with the Nusselt number the quantity $\overline{v_z\theta}$ (where the overbar symbol denotes the volume average) will often be used to characterize the state of the system. In the following we shall loosely refer to $\overline{v_z\theta}$ as reduced Nusselt number.

3. Numerical method

The evolution equations (2.6), (2.8) for the hydrodynamic variables are solved using a pseudospectral numerical method based on Fourier series in the horizontal directions x and y and a Chebyshev polynomial expansion in the vertical z-direction (Canuto *et al.* 1988; Gottlieb & Orszag 1977). Because of incompressibility, only two velocity components are independent. The velocity field can be represented in terms of two scalar quantities Ψ and Φ using the poloidal–toroidal decomposition (Thual 1992)

$$\boldsymbol{v}(x, y, z, t) = \nabla\times(\nabla\times\boldsymbol{e}_z\Phi(x, y, z, t)) + \nabla\times\boldsymbol{e}_z\Psi(x, y, z, t). \tag{3.1}$$

Equations for Φ and Ψ are derived by taking the curl and twice the curl of the momentum equation and projection onto the vertical direction. We obtain two equations for the vertical velocity component $v_z = -\Delta_h\Phi$ and the vertical vorticity component $\omega_z = -\Delta_h\Psi$, where $\Delta_h = \partial_x^2 + \partial_y^2$ denotes the horizontal Laplace operator. The quantities v_z and ω_z determine the velocity field up to a mean flow $U(z)\boldsymbol{e}_x + V(z)\boldsymbol{e}_y$. Equations for U and V are obtained by averaging the momentum equation over horizontal cross-sections of the periodicity domain. The complete system of evolution equations reads

$$\partial_t\omega_z - \boldsymbol{e}_z\cdot\nabla\times(\boldsymbol{v}\times\boldsymbol{\omega}) = \nabla^2\omega_z, \tag{3.2}$$

$$\partial_t\nabla^2 v_z + \partial_z\nabla\cdot(\boldsymbol{v}\times\boldsymbol{\omega}) - \boldsymbol{e}_z\cdot\nabla^2(\boldsymbol{v}\times\boldsymbol{\omega}) = \nabla^4 v_z, \tag{3.3}$$

$$P(\partial_t\theta + (\boldsymbol{v}\cdot\nabla)\theta) = \nabla^2\theta + v_z, \tag{3.4}$$

$$\partial_t U + \partial_z\langle v_x v_z\rangle = \partial_z^2 U, \tag{3.5}$$

$$\partial_t V + \partial_z\langle v_y v_z\rangle = \partial_z^2 V, \tag{3.6}$$

where the angular brackets $\langle\ \rangle$ denote horizontal averages. The boundary conditions at the free surface are

$$\partial_z^2 v_z - Ma\,\Delta_h\theta = v_z = \partial_z\omega_z = \partial_z\theta = \partial_z U = \partial_z V = 0 \quad \text{at } z = 1, \tag{3.7}$$

where $\boldsymbol{\nabla}\cdot\boldsymbol{v} = 0$ has been used in the derivation of the first (Marangoni) boundary condition. For the boundary conditions at the bottom we have to distinguish the free-slip and no-slip cases. Only the conditions

$$v_z = \theta = 0 \quad \text{at } z = 0 \tag{3.8}$$

are unaffected by the particular choice. The other conditions at $z = 0$ read

$$\partial_z^2 v_z = \partial_z\omega_z = \partial_z U = \partial_z V = 0 \quad \text{(free-slip)}, \tag{3.9}$$

$$\partial_z v_z = \omega_z = U = V = 0 \quad \text{(no-slip)}. \tag{3.10}$$

Integrating the mean flow components U and V with respect to z gives scalar quantities

$$Q_x = \int_0^1 U(z)\,\mathrm{d}z, \qquad Q_y = \int_0^1 V(z)\,\mathrm{d}z, \tag{3.11}$$

which represent the components of the normalized linear momentum in the x- and y-directions up to prefactors. They can also be regarded as dimensionless mass fluxes in x or y, which are additionally normalized to the unit square. For free-slip boundary conditions the linear momentum is conserved, i.e. Q_x and Q_y remain unchanged in the time evolution. In the simulations with free-slip boundary conditions we take $Q_x = Q_y = 0$ without loss of generality.

In order to derive the discrete representation of (3.2)–(3.4) we put $\zeta = \omega_z$, $\eta = \Delta v_z$, $\xi = v_z$ and introduce $\zeta_{\boldsymbol{k}}$, $\eta_{\boldsymbol{k}}$, $\xi_{\boldsymbol{k}}$ and $\theta_{\boldsymbol{k}}$ as the Fourier coefficients to the wave vector $\boldsymbol{k} = k_x\boldsymbol{e}_x + k_y\boldsymbol{e}_y$. For time differencing we use the implicit backward Euler scheme for the linear terms and the explicit second-order Adams–Bashforth scheme for nonlinear terms. Advancing the solution from time level n to $n+1$ then requires the solution of four linear second-order boundary value problems for each wave vector. They read

$$\left(\mathrm{D}^2 - \boldsymbol{k}^2 - \frac{1}{\Delta t}\right)\zeta_{\boldsymbol{k}}^{n+1} = -\frac{\zeta_{\boldsymbol{k}}^n}{\Delta t} - \mathrm{AB}\left\{[\boldsymbol{e}_z\cdot\boldsymbol{\nabla}\times(\boldsymbol{v}\times\boldsymbol{\omega})]_{\boldsymbol{k}}\right\}^n, \tag{3.12}$$

$$\left(\mathrm{D}^2 - \boldsymbol{k}^2 - \frac{1}{\Delta t}\right)\eta_{\boldsymbol{k}}^{n+1} = -\frac{\eta_{\boldsymbol{k}}^n}{\Delta t} + \mathrm{AB}\left\{\left[\partial_z\boldsymbol{\nabla}\cdot(\boldsymbol{v}\times\boldsymbol{\omega}) - \boldsymbol{e}_z\cdot\nabla^2(\boldsymbol{v}\times\boldsymbol{\omega})\right]_{\boldsymbol{k}}\right\}^n, \tag{3.13}$$

$$\left(\mathrm{D}^2 - \boldsymbol{k}^2\right)\xi_{\boldsymbol{k}}^{n+1} - \eta_{\boldsymbol{k}}^{n+1} = 0, \tag{3.14}$$

$$\left(\mathrm{D}^2 - \boldsymbol{k}^2 - \frac{P}{\Delta t}\right)\theta_{\boldsymbol{k}}^{n+1} + \xi_{\boldsymbol{k}}^{n+1} = P\left(-\frac{\theta_{\boldsymbol{k}}^n}{\Delta t} + \mathrm{AB}\left\{[\boldsymbol{v}\cdot\boldsymbol{\nabla}\theta]_{\boldsymbol{k}}\right\}^n\right), \tag{3.15}$$

with $\mathrm{D} = \mathrm{d}/\mathrm{d}z$ and $\mathrm{AB}\{f\}^n = (3f^n - f^{n-1})/2$ from the Adams–Bashforth formula. For the mean flow components U and V, time differencing gives

$$\left(\mathrm{D}^2 - \frac{1}{\Delta t}\right)U^{n+1} = -\frac{U^n}{\Delta t} + \mathrm{AB}\left\{\frac{\partial}{\partial z}\langle v_x v_z\rangle\right\}^n, \tag{3.16}$$

$$\left(\mathrm{D}^2 - \frac{1}{\Delta t}\right)V^{n+1} = -\frac{V^n}{\Delta t} + \mathrm{AB}\left\{\frac{\partial}{\partial z}\langle v_y v_z\rangle\right\}^n. \tag{3.17}$$

The boundary conditions for the Fourier coefficients are identical to (2.9) and either

(2.10) or (2.11) with exception of the Marangoni boundary condition, which becomes

$$\eta_k + Ma\boldsymbol{k}^2\theta_k = 0. \tag{3.18}$$

An inspection of the system of equations and of the boundary conditions shows that the equations for ζ_k and the mean flow components U, V are independent of the other equations. They can be solved directly since suitable boundary conditions are available. The equations for η_k, ξ_k and θ_k are coupled because of the Marangoni boundary condition. With η_k given, we can compute ξ_k and θ_k in turn. We solve these coupled equations by computing two linearly independent solutions of the homogeneous system for η_k, i.e. we represent solutions as

$$\eta_k = \eta_k^{(0)} + \lambda\eta_k^{(1)} + \mu\eta_k^{(2)}, \tag{3.19}$$

$$\xi_k = \xi_k^{(0)} + \lambda\xi_k^{(1)} + \mu\xi_k^{(2)}, \tag{3.20}$$

$$\theta_k = \theta_k^{(0)} + \lambda\theta_k^{(1)} + \mu\theta_k^{(2)}, \tag{3.21}$$

where the functions with superscript (0) satisfy the inhomogeneous equations (3.13)–(3.15) and the boundary conditions $\eta_k^0 = 0$ at $z = 0$ and $z = 1$. The solutions with superscripts (1) and (2) are obtained from the solution of the homogeneous equations ((3.13)–(3.15) with zero right-hand sides) with two linearly independent boundary conditions on η_k. We take

$$\eta_k^{(1)}(1) = \eta_k^{(1)}(0) = 1, \tag{3.22}$$

$$\eta_k^{(2)}(1) = -\eta_k^{(2)}(0) = 1. \tag{3.23}$$

The unknown coefficients λ and μ are determined by inserting the above expressions into the Marangoni and the no-slip/free-slip boundary condition at the bottom.

In the numerical simulations the size Δt of the time step is fixed. The auxiliary functions $\eta_k^{(1,2)}$, $\xi_k^{(1,2)}$ and $\theta_k^{(1,2)}$ only have to be computed once at the start for each wave vector $\boldsymbol{k}$. They are stored and reused at every time step.

In the discrete Chebyshev representation each of the boundary value problems (3.12)–(3.17) for the z-dependent Fourier coefficients at time level $n + 1$ reduces to a tridiagonal system of linear algebraic equations. The boundary conditions are incorporated by means of the τ-method, which results in two filled rows. Nonlinear terms are computed pseudospectrally, i.e. in physical space using fast Fourier and fast Chebyshev transforms.

The algorithm is parallelized by assigning slices of the wave vector array to the individual processors. The array is sliced in the x-direction so that the wave vectors assigned to an individual processor cover some x-wavenumber range and the entire range of y-wavenumbers. By that, only the Fourier transforms require inter-process communication. We compute them by the transpose method (Jackson, She & Orszag 1991). The program can be executed on a number of processors which is a power of two and which is smaller than the number of collocation points with respect to the x- and y-directions. We have chosen C as programming language and MPI as communication library. At a resolution of $64 \times 64 \times 33$ a single time step takes 0.2 s when the program runs on 16 processors of a SGI Origin 2000 computer (13 Fourier transforms per time step, speedup is 13.9 when compared with sequential program execution).

Several independent tests were performed for validation of the numerical code. The first is based on linear stability analysis of the basic conductive state. We compare the growth rate β obtained from a numerical simulation with zero nonlinear terms with

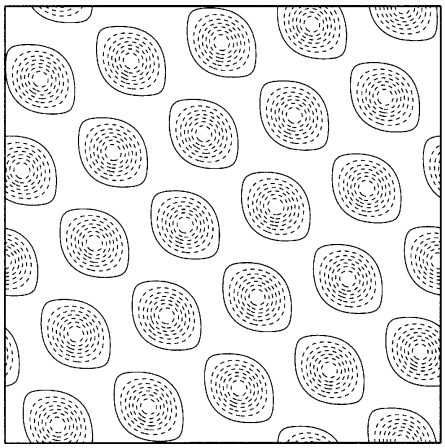

FIGURE 1. Contour plot of the surface temperature perturbation θ with free-slip boundary conditions for $P = 0$, $Ma = 58$. Aspect ratio is $L_x = L_y = 20$. Dashed lines correspond to negative values of θ, i.e. fluid descends from the surface in the centre of the hexagon. Notice the skewed shape of the hexagons. Numerical resolution is $128 \times 128 \times 17$ collocation points in x, y and z.

the exact value from linear stability analysis. By that, we verify the proper computation of v_z and θ. For free-slip boundary conditions and $Ma = 70$, $P = 0.1$, $k = 1.7$ the exact result reads $\beta_{ex} = 2.30063$, whereas the simulation gives $\beta_{sim} = 2.30089$. For no-slip boundary conditions and $Ma = 85$, $P = 0.5$, $k = 2.0$ we find $\beta_{ex} = 0.53133$, which differs only slightly from $\beta_{sim} = 0.53145$.

We have also verified the proper computation of the vertical vorticity with nonlinear terms turned off. The vertical vorticity was initialized with $\zeta = \cos(\pi(1-z)/2)\cos(x)$ and the decay rate $\beta = -(\pi^2/4+1)$ of this mode was also verified with a relative error of about 10^{-4} (no-slip case). All these tests were performed with $N_z = 33$ collocation points and a time step $\Delta t = 10^{-4}$.

The proper computation of the nonlinear terms can be checked in simulations of RBC between no-slip walls at zero Prandtl number. We can adapt our code to this situation by including the buoyancy term and changing the boundary conditions. For comparison we employ results for the bifurcation from straight rolls to travelling wave convection reported by Thual (1992). Using the same numerical resolution, our data for the measured mean square of the velocity component parallel to the roll axis for the travelling wave case at Rayleigh numbers $Ra \approx 1900$ differ by less than 1% from the values given in table 2 of Thual's paper.

4. Results for free-slip boundary conditions

4.1. *Transition to time-dependent convection*

We shall first consider the case of free-slip boundary conditions at the bottom of the layer. Although it is somewhat less realistic than the no-slip case, it seems appropriate to examine it in the three-dimensional setting in order to compare with previous two-dimensional simulations by the authors. A similar approach has been taken by Thual (1992) in numerical simulations of RBC at low Prandtl number.

Linear stability theory of the basic conductive state predicts instability above a critical Marangoni number $Ma_c = 57.598$ with a corresponding critical wavenumber $k_c = 1.7003$ at zero Biot number (Boeck & Thess 1997). As in the case of a no-slip

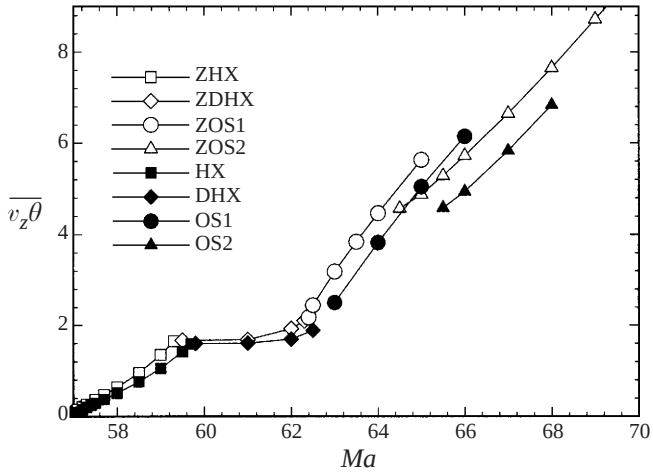

FIGURE 2. Partial bifurcation diagram for free-slip boundary conditions in the basic cell with $L_x = 4\pi/k_c$ and $L_y = 4\pi/\sqrt{3}k_c$. Abbreviations used for the different branches indicate zero Prandtl number with the initial letter Z, otherwise $P = 0.005$. HX denotes perfect hexagons, DHX deformed hexagons. OS identifies oscillatory solutions. The different oscillatory states distinguished by the digits 1 or 2 are explained in the text. The numerical values for the reduced Nusselt number $\overline{v_z\theta}$ are maximum values during the oscillations.

bottom we expect and observe 'inverted' hexagonal cells at the onset of convection (Thess & Bestehorn 1995). Figure 1 shows the surface temperature perturbation θ in the final state for $Ma = 58$ and $P = 0$ in a square domain of aspect ratio $L_x = L_y = 20$. The simulation has been started with random initial conditions of small amplitude. Notice that the pattern is distorted, and that the centres of the hexagons are cold, i.e. fluid descends back into the volume after giving off heat. The distortion can be attributed to the incompatibility of the square domain with the symmetry of a perfect hexagonal pattern (Matthews 1998), but the hexagons have a distinctly skewed shape in contrast to the case of high Prandtl number (Thess & Orszag 1995). In spite of the distortion, the number of hexagons is close to what can be expected on the basis of linear stability theory. According to the Christopherson solution (Chandrasekhar 1961), the area occupied by a hexagonal cell is

$$A_c = \frac{8\pi^2}{\sqrt{3}k_c^2}, \tag{4.1}$$

giving $L_x L_y / A_c = 25.3$. The actual number of cells in figure 1 is 24, which demonstrates that the proper wavelength is selected.

Since the objective of this work is the investigation of moderately or strongly nonlinear convection, we shall now replace the large aspect ratio with a small domain for a systematic investigation of the flows emerging upon increasing Ma. We select the smallest possible aspect ratios $L_x = 4\pi/k_c$, $L_y = 4\pi/\sqrt{3}k_c$ compatible with the hexagonal planform. This domain accommodates two hexagons with the critical basic wavenumber. In the following, we shall investigate the case of zero Prandtl number as well as a finite Prandtl number $P = 0.005$. This value is approximately equal to that of liquid sodium, the liquid metal with the lowest Prandtl number.

In our simulations we have systematically increased Ma by starting new runs with initial velocity and temperature data from previous runs for smaller Ma. Occasionally, we have also started with random initial conditions to check that we are not missing

	Ma	Planform	E	$\overline{v_z\theta}$	N_x	N_y	N_z	Δt
(*a*)	57.5	HX	175	0.373	32	32	17	n/a
	58	HX	299	0.639	32	32	17	n/a
	59	HX	632	1.35	64	32	33	n/a
	60	DHX	789	1.67	64	32	33	n/a
	61	DHX	808	1.68	64	32	33	n/a
	62	DHX	933	1.93	32	32	33	n/a
	63	OS1	1560	3.19	32	32	33	4×10^{-4}
	64	OS1	2210	4.47	32	32	33	3×10^{-4}
	65	OS1	2810	5.63	32	32	33	3×10^{-4}
	65	OS2	2450	4.88	32	32	33	3×10^{-4}
	66	OS2	2910	5.72	64	32	33	3×10^{-4}
	68	OS2	3990	7.65	64	32	33	2.5×10^{-4}
	70	OS2	5220	9.78	64	32	33	2.5×10^{-4}
(*b*)	57.5	HX	138	0.295	64	32	17	n/a
	58	HX	240	0.514	64	32	17	n/a
	59	HX	493	1.06	64	32	17	n/a
	60	DHX	753	1.60	64	32	17	n/a
	61	DHX	768	1.61	32	32	17	n/a
	62	DHX	819	1.70	32	32	17	n/a
	63	OS1	1220	2.50	32	32	33	3×10^{-4}
	64	OS1	1880	3.82	32	32	33	3×10^{-4}
	65	OS1	2500	5.04	32	32	33	3×10^{-4}
	66	OS1	3070	6.14	64	32	33	2×10^{-4}
	67	OS2	2980	5.83	64	32	33	2×10^{-4}
	68	OS1	4040	7.93	64	32	33	2×10^{-4}
	68	OS2	3510	6.84	64	32	33	2.5×10^{-4}

TABLE 1. Numerical data from simulations with (*a*) $P = 0$ and (*b*) $P = 0.005$, and free-slip boundary conditions at the bottom of the layer. E stands for the kinetic energy of the flow in the basic cell, $\overline{v_z\theta}$ denotes the volume average of $v_z\theta$. For oscillatory solutions the numerical values are maxima attained in the cycles. N_x, N_y and N_z denote the number of collocation points in x, y and z. The time step Δt is only given for time-dependent flows. HX denotes perfect hexagons, DHX deformed hexagons. OS identifies oscillatory solutions. The different oscillatory states distinguished by the digits 1 or 2 are explained in the main text.

new solution branches. However, we cannot rule out that some have been overlooked in our study. During the runs, integral quantities such as the kinetic energy and the reduced Nusselt number were monitored. For convergence towards stationary solutions, the runs were usually terminated when both quantities were changing only in the fourth decimal place over a typical monitoring interval of 50 time steps. In general, the runs were continued at least up to $t = 10 \ldots 20$. Figure 2 shows a partial summary of our simulation results for both zero and finite Prandtl number, namely the solution branches obtained up to onset of chaos. Tables 1(*a*) and 1(*b*) list some data which may be useful for future comparison.

Generally, hexagons set in subcritically. According to our numerical simulations the subcritical range extends down to $Ma_s = 57.04$ for $P = 0$. This is significantly less than the threshold $Ma_c = 57.598$ for linear instability of the conductive state. For $P = 0.005$ the convective state persists down to a Marangoni number Ma_s less than or equal to 57.10. The size $(Ma_c - Ma_s)/Ma_c \approx 1\%$ of the subcritical range is about the same as for infinite Prandtl number (Thess & Orszag 1995). The apparent decrease in size of the subcritical range when going from zero to finite Prandtl number

	Ma	Planform	E	$\overline{v_z\theta}$	N_x	N_y	N_z	Δt
(*a*)	80	HX	77	0.201	64	32	17	n/a
	82	HX	171	0.451	64	32	17	n/a
	86	HX	361	0.970	64	32	17	n/a
	88	DHX	431	1.12	64	16	17	n/a
	90	DHX	469	1.18	64	32	17	n/a
	92	DHX	470	1.15	64	32	17	n/a
	95	R	490	1.19	32	n/a	17	n/a
	95	TW	511	1.23	64	32	33	4×10^{-4}
	100	R	722	1.73	64	n/a	17	n/a
	100	TW	829	1.97	64	32	33	1.5×10^{-4}
	105	TW	1180	2.78	64	32	33	2×10^{-4}
	106	R	1080	2.56	64	n/a	33	n/a
	110	TR	2850	6.30	64	n/a	33	1×10^{-4}
	115	TR	11260	19.6	64	n/a	33	1×10^{-4}
	120	OTW	14740	25.2	128	32	33	1×10^{-4}
	125	OTW	14910	26.0	128	64	33	7×10^{-5}
(*b*)	80	HX	68	0.177	64	32	17	n/a
	82	HX	154	0.407	64	32	17	n/a
	86	HX	328	0.879	64	32	17	n/a
	88	DHX	398	1.03	64	32	17	n/a
	90	DHX	440	1.11	64	32	17	n/a
	92	DHX	455	1.11	64	32	17	n/a
	95	R	467	1.13	32	n/a	17	n/a
	95	TW	480	1.16	64	16	17	5×10^{-4}
	100	TW	779	1.85	64	16	17	5×10^{-4}
	102	R	784	1.87	32	n/a	17	n/a
	105	TW	1110	2.60	64	16	17	5×10^{-4}
	110	TR	2050	4.71	64	n/a	33	2×10^{-4}
	115	TR	7500	13.8	64	n/a	33	1×10^{-4}
	120	OTW	14960	25.1	128	32	33	8×10^{-5}
	122	OTW	15080	25.4	128	32	33	7×10^{-5}

TABLE 2. Numerical data from simulations with (*a*) $P = 0$ and (*b*) $P = 0.005$, and no-slip boundary conditions at the bottom of the layer. E stands for the kinetic energy of the flow in the basic cell, $\overline{v_z\theta}$ denotes the volume average of $v_z\theta$. N_x, N_y and N_z denote the number of collocation points in x, y and z. The time step Δt is only given for time-dependent flows. HX denotes perfect hexagons, DHX deformed hexagons, TW identifies travelling waves and R identifies steady rolls. Travelling rolls are abbreviated as TR and oblique travelling waves as OTW.

may be related to the fact that the nonlinear term in the heat equation contributes to nonlinear saturation. The corresponding reduction in flow amplitude would lead to a breakdown of convection at a higher Ma if the minimum amplitude needed for sustaining convection remained approximately constant.

Figure 3(*a–d*) illustrates the first, symmetry-breaking bifurcation of the hexagonal pattern, which occurs around $Ma \approx 59.5$. The new stationary cell pattern will be referred to as deformed hexagons. It does not retain the hexagonal symmetry but has reflection symmetries with respect to both x- and y-directions (after suitably translating the pattern in x and y). This can be seen in the striking change of the surface vorticity plots of figure 3(*b*, *d*). Moreover, the amplitude of the vertical vorticity is larger by two orders of magnitude in figure 3(*d*) than in figure 3(*b*).

The qualitative difference between the two patterns can also be described in Fourier space. For the surface temperature distribution of figure 3(*a*) the wave

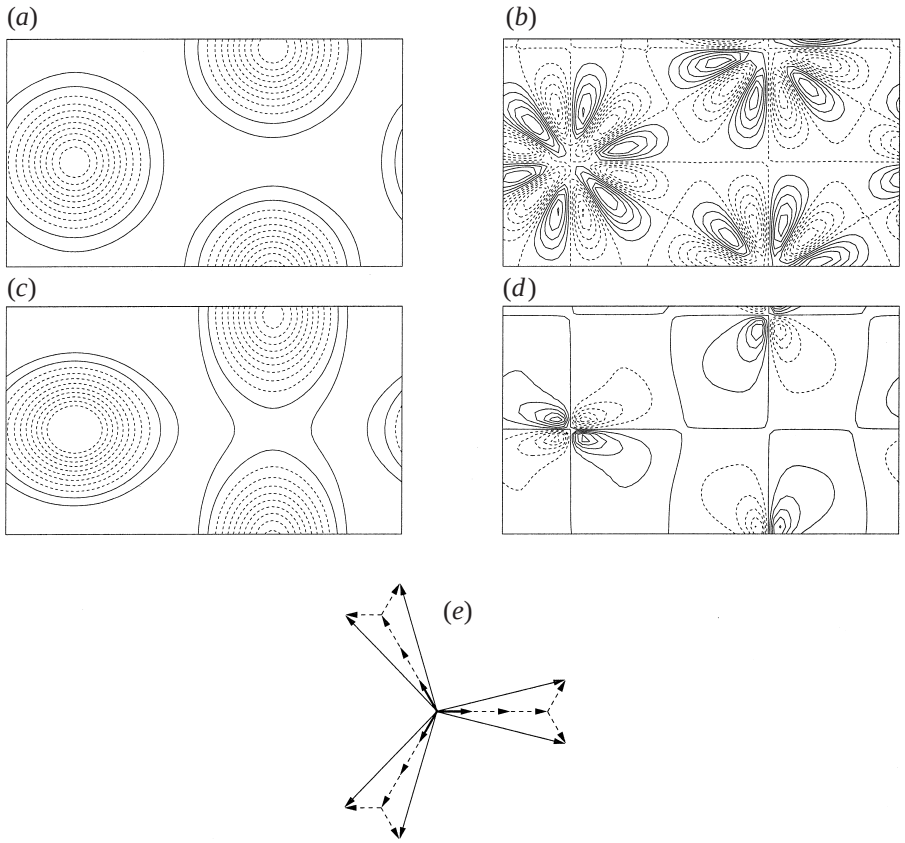

FIGURE 3. Free-slip boundary conditions with $P = 0$ in the basic cell: (a, c) surface temperature perturbation θ and (b, d) surface vorticity for $Ma = 59$ (a, b) and for $Ma = 60$ (c, d). Wave vectors of length $\sqrt{13}k_c$ contributing to the pattern (b) can be constructed from the basic triplet (bold arrows) as shown in (e).

vectors contributing to the pattern ('excited' wave vectors) are essentially only those of the basic triplet. This is no longer the case in figure 3(c), where additional wave vectors outside the basic triplet also have a significant amplitude, although the triplet is still dominant. In the surface vorticity plot of figure 3(b), six wave vectors of length $\sqrt{13}k_c$ are excited. The amplitudes associated with each of these vectors are equal in modulus. We remark that these vectors are integer linear combinations of vectors taken from the basic triplet. Figure 3(e) shows how these vectors are constructed. By contrast, in the surface vorticity distribution of figure 3(d) there are wave vectors of length k_c excited, which constitutes an essential feature of this bifurcation.

We further note that the convective heat transport characterized by the reduced Nusselt number $\overline{v_z\theta}$ remains almost constant for the deformed hexagons. The same applies for other integral quantities such as the kinetic energy. We also remark that the perfect hexagons (and thus the bifurcation to deformed hexagons) will be absent when the aspect ratio does not admit them as in figure 1.

Time-dependent convection sets in via an oscillatory instability. Figure 4(a–c) illustrates the dynamics for the case $Ma = 63$, $P = 0$, while figure 4(d) shows the corresponding evolution of the heat transport over one oscillation period. The low energy state of figure 4(a) corresponds to a pattern where the cells have shrunk to a

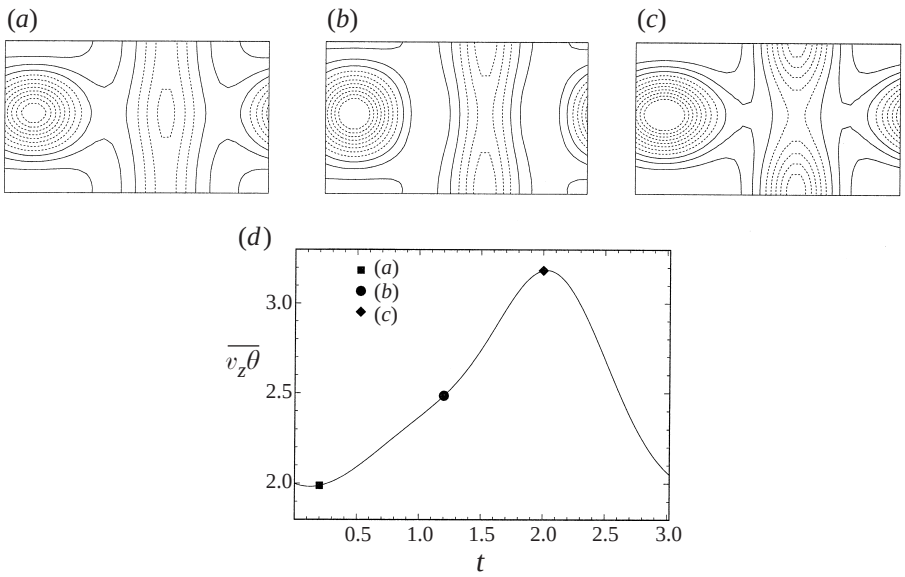

FIGURE 4. Free-slip boundary conditions with $P = 0$ and $Ma = 63$ in the basic cell. (*a–c*) Snapshots of the surface temperature perturbation θ. (*d*) Evolution of the reduced Nusselt number $\overline{v_z\theta}$ during a single oscillation period.

minimal size, which allows the formation of a roll-like structure. As time progresses, the cells expand, and the roll converts into individual cells. After reaching a peak in the energy (as well as in the Nusselt number), the cells shrink and the roll reappears. The effective rise in the heat transport for the oscillating branches ZOS1 ($P = 0$) and OS1 ($P = 0.005$) is somewhat exaggerated in figure 2 since we have plotted the peak values attained during the oscillation and not the temporal average. For an explanation of the abbreviations see the caption of figure 2.

The next instability is associated with excitations of the mean flow component V, which is still zero in the simple oscillatory regime just described. The new state with non-zero V occurs after a period-doubling bifurcation. A lateral oscillation with respect to the short dimension of the cell with half the frequency of the contraction/expansion now overlays the basic oscillation. The corresponding branches denoted by ZOS2 and OS2 in figure 2 overlap with ZOS1 and OS1. At somewhat higher Ma, the zero mode oscillations then undergo a period doubling themselves, which leads to a lateral drift of the pattern as a whole. For $P = 0$ this happens at a Marangoni number in the interval $66 < Ma < 67$. The drift motion occurs in the y-direction, i.e. parallel to the shorter side of the cell. It becomes apparent as a splitting of a periodic orbit in the phase plot of the toroidal kinetic energy E_t vs. the total kinetic energy E in figure 5(*a*). The toroidal kinetic energy is defined as the energy associated with the toroidal part $\nabla \times \boldsymbol{e}_z \Psi$ of the velocity field including the mean flow components U and V, i.e.

$$E_t = \frac{1}{2} \int_0^{L_x} \int_0^{L_y} \int_0^1 |\nabla \times \boldsymbol{e}_z \Psi + U \boldsymbol{e}_x + V \boldsymbol{e}_y|^2 \, \mathrm{d}x \, \mathrm{d}y \, \mathrm{d}z. \tag{4.2}$$

Figure 5(*b*) shows another period doubling at $Ma = 70.5$ for $P = 0$. The qualitative behaviour is the same for $P = 0.005$, but the motion shown in figure 5(*b*) has already occurred at $Ma = 68$. Based on these observations one could speculate

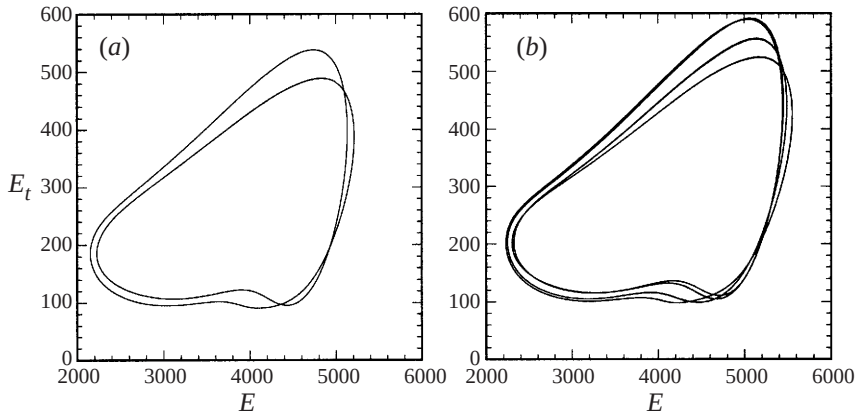

FIGURE 5. Free-slip boundary conditions with $P = 0$ in the basic cell. Phase plot of the toroidal part E_t of the kinetic energy vs. the total kinetic energy E for (*a*) $Ma = 70$, (*b*) $Ma = 70.5$.

about a period-doubling cascade leading to temporal chaos. However, we have not attempted to search for orbits with even longer periods since the long integration times ($t_{run} > 100$) make these simulations very expensive.

4.2. *Regularity of the zero-Prandtl-number limit*

In two-dimensional simulations with free-slip boundary conditions it turns out that the case $P = 0$ leads to a singular behaviour of the system above a certain inertial Marangoni number Ma_i, which is $Ma_i \approx 73$ for a periodicity length $L_x = 2\pi/k_c$ (Boeck & Thess 1997). For $Ma > Ma_i$ the system no longer evolves into a steady state. Instead, the flow amplitude grows exponentially without bound. Unbounded growth cannot occur when the Prandtl number is finite. The reason for this is that for $P = 0$ the temperature perturbation does not perturb the linear conductive profile. For $P > 0$ this is no longer the case, and the temperature perturbation is now a bounded quantity because of the finite applied temperature gradient and the fact that no heat is generated inside the fluid. However, in order for this effect to provide a mechanism of saturation, the velocity must be of the order of the thermal scale κ/d which indicates the singular nature of the limit $P \to 0$. The associated mode of convection is called inertial or flywheel convection.

Inertial convection is clearly an admissible state of the system when $Ma > Ma_i$ and $P > 0$. Nevertheless it will be irrelevant for the actual behaviour in three dimensions at low P if finite energy solutions prevail for $P = 0$ and $Ma > Ma_i$, i.e. if the limit $P \to 0$ is regular in three dimensions. Simulations with $P = 0$ performed for $Ma = 80$ in the geometry accommodating two hexagons did not exhibit unbounded growth or any tendency towards a two-dimensional state. However, these observations do not rule out that the inertial mode may still be reached by the dynamics. To exclude this possibility we need to show that the exponentially growing roll solutions are unstable with respect to three-dimensional perturbations. We have therefore performed simulations in a square domain of aspect ratio $L_x = L_y = 2\pi/k_c$ for $P = 0$. The initial condition consisted of a pair of stationary rolls parallel to the y-direction with $P = 0.1$, $Ma = 80$ as considered in Boeck & Thess (1997). Setting $P = 0$ gives an exponentially growing solution in two dimensions. For the three-dimensional simulations we have added a small random perturbation to ω_z.

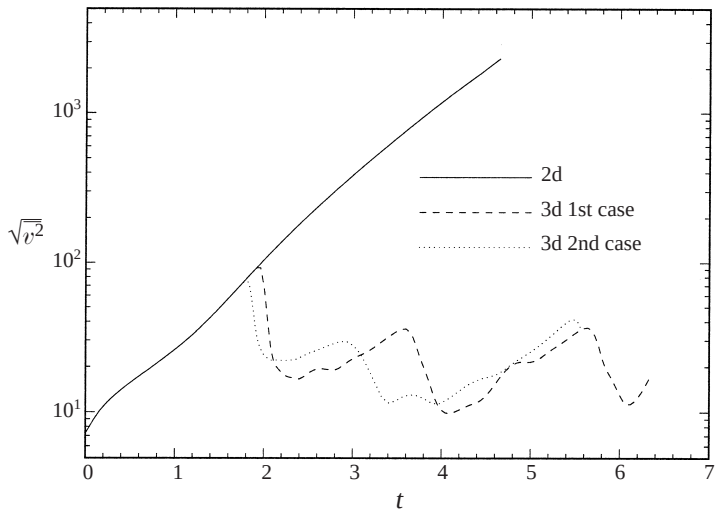

FIGURE 6. Stability of the exponentially growing two-dimensional roll solution for free-slip conditions. Parameters are $L_x = L_y = 2\pi/k_c$, $Ma = 80$, $P = 0$. The exponential growth of the flow amplitude (measured by the mean-square velocity) eventually breaks down when three-dimensional perturbations are present. The breakdown occurs earlier when the amplitude of the random perturbation added to ω_z is larger (1st case).

The mean square velocity as a function of time is plotted in figure 6. The curves for the purely two-dimensional and the two three-dimensional cases are indistinguishable up to a point where the two-dimensional rolls break down into a three-dimensional pattern. The two three-dimensional cases are characterized by a different magnitude of the random perturbation to ω_z, which is larger for the second case. On the basis of these results we can conjecture that the exponentially growing roll solutions will be unstable in three dimensions and that inertial convection therefore does not occur unless the system is kept in a two-dimensional state through additional measures.

The degree of two-dimensionalization of the flow at the free surface was monitored by means of a scalar diagnostic quantity W. The definition of W is inspired by experimental work (Gollub & McCarriar 1982) on the wavenumber distributions of convective patterns. It rests on the two-dimensional power spectrum of the surface temperature perturbation θ_s. Because θ_s is a real function, the power spectrum $|\theta_s(\boldsymbol{k})|^2$ is symmetric with respect to $\boldsymbol{k} \to -\boldsymbol{k}$, i.e. we can restrict our consideration to the half-plane $k_x < 0$, say. If the flow is two-dimensional, then the power spectrum $|\theta_s(\boldsymbol{k})|^2$ collapses to a line in this half-plane through the origin. W should characterize the deviation from this linear distribution. We shall measure the deviation relative to the centre of mass $\boldsymbol{k}_m$, which is defined by

$$\boldsymbol{k}_m = \frac{\displaystyle\int_{k_x<0} |\theta_s(\boldsymbol{k})|^2 \boldsymbol{k}\, \mathrm{d}k_x\, \mathrm{d}k_y}{\displaystyle\int_{k_x<0} |\theta_s(\boldsymbol{k})|^2\, \mathrm{d}k_x\, \mathrm{d}k_y}. \tag{4.3}$$

We denote by $l_m(\boldsymbol{k})$ the minimum distance between the point $\boldsymbol{k}$ and the line passing through the origin and the centre of mass $\boldsymbol{k}_m$ as plotted in figure 7. The diagnostic

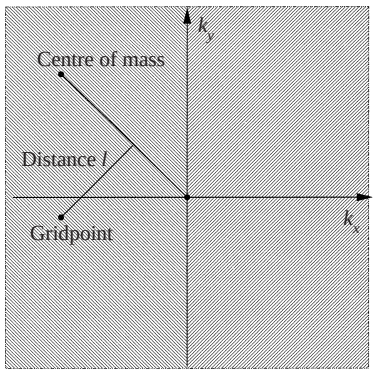

FIGURE 7. Schematic diagram of the Fourier space distance l used in defining the diagnostic quantity W.

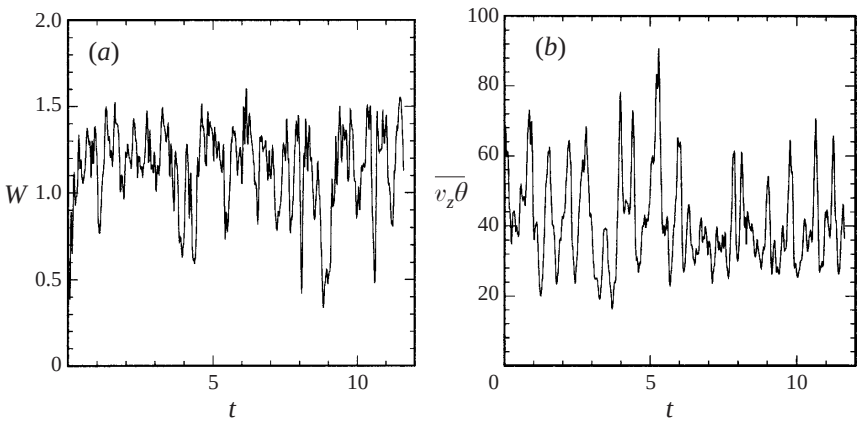

FIGURE 8. Free-slip boundary conditions with $P = 0$, $Ma = 120$ in the basic cell. (*a*) Time series of W demonstrates the persistent three-dimensionality of the flow. (*b*) Chaotic time dependence of the reduced Nusselt number $\overline{v_z\theta}$. Numerical resolution is $128 \times 64 \times 33$ collocation points for this run.

quantity W can now be defined as

$$W = \frac{\displaystyle\int_{k_x<0} |\theta_s(\boldsymbol{k})|^2 l_m(\boldsymbol{k})\,\mathrm{d}k_x\,\mathrm{d}k_y}{\displaystyle\int_{k_x<0} |\theta_s(\boldsymbol{k})|^2\,\mathrm{d}k_x\,\mathrm{d}k_y}. \tag{4.4}$$

W is clearly non-negative and becomes zero only for purely two-dimensional rolls. Large values of W can be attained when large excited wave vectors of different orientations exist, i.e. for three-dimensional surface temperature distributions with pronounced small-scale structures.

In conclusion of the free-slip case we shall now return to the periodic domain with $L_x = 4\pi/k_c$, $L_y = 4\pi/\sqrt{3}k_c$ considered before. We have performed additional simulations for Marangoni numbers up to $Ma = 120$. Figure 8(*a*) shows the temporal evolution of W at $Ma = 120$ and $P = 0$. Values of order unity for W demonstrate the persistent three-dimensional character of this flow and indicate the absence of small-scale structures in the surface temperature distribution. The chaotic time evolution

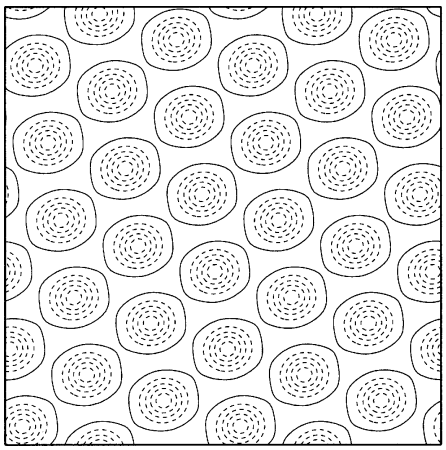

FIGURE 9. Contour plot of θ at the free surface with no-slip conditions for $P = 0$, $Ma = 80$. Aspect ratio is $L_x = L_y = 20$. Dashed lines correspond to negative values of θ. Notice the skewed shape of the hexagons. Numerical resolution is $128 \times 128 \times 17$ collocation points in x, y and z.

of the heat flux is shown in figure 8(*b*). The same qualitative behaviour was also observed in the case with $P = 0$ and $Ma = 100$.

5. Results for no-slip boundary conditions

5.1. *Transition to time-dependent convection*

The linear stability threshold in the no-slip case is given by the classical result of Pearson (1958). For our case ($Bi = 0$) it is $k_c = 1.9929$ and $Ma_c = 79.607$. We have again performed a single simulation with large aspect ratio $L_x = L_y = 20$ in order to verify the selection of the proper wavenumber near the instability threshold by our numerical code. Figure 9 is a plot of the surface temperature perturbation in the final state after starting from random initial conditions of small amplitude. Notice again the incompatibility of the square domain with the symmetry of the hexagonal pattern causing distortion. The simple estimate $L_x L_y / A_c = 34.8$ from equation (4.1) for the number of cells is in good agreement with the actual number of 34.

As in the previous section, we shall now study the flow in the smallest possible rectangular domain compatible with hexagonal cells. This domain has $L_x = 4\pi/k_c$, $L_y = 4\pi/\sqrt{3}k_c$. It accommodates two hexagons with the critical basic wavenumber. As before, we shall investigate the case of zero Prandtl number as well as a finite Prandtl number $P = 0.005$. Figure 10(*a*) shows a partial summary of our simulation results for both zero and finite Prandtl number, and tables 2(*a*) and 2(*b*) give the corresponding data.

The subcritical range of the perfect hexagons extends down to $Ma_s = 79.05$ for $P = 0$. For $P = 0.005$ the convective state persists down to a Marangoni number Ma_s less than or equal to 79.10. The size $(Ma_c - Ma_s)/Ma_c \approx 0.8\%$ of the subcritical range is slightly smaller than for the free-slip bottom. Perfectly hexagonal cells are stable up to $Ma \approx 86$, i.e. they occur over a significantly wider range of Marangoni numbers than for a free-slip bottom. This may be due to the slower increase of the flow amplitude with Ma than in the free-slip case (cf. tables) caused by the additional friction at the bottom. The insets in figure 10(*a*) show the surface temperature distribution of deformed hexagons replacing the hexagons beyond $Ma \approx 86$. As for

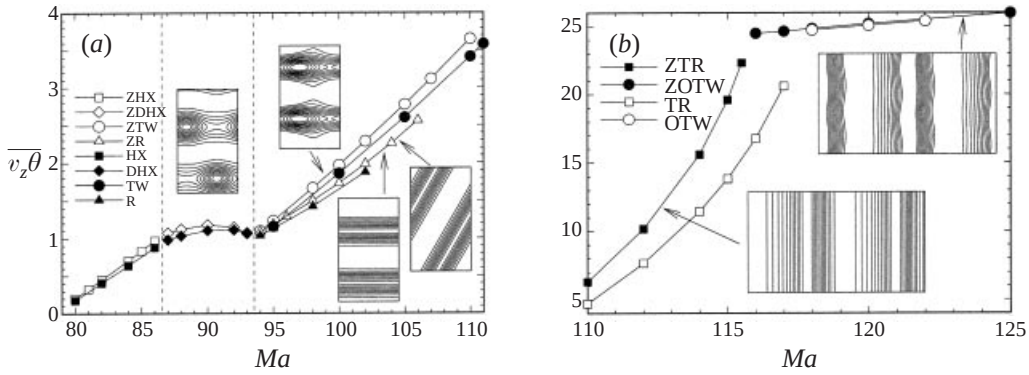

FIGURE 10. Bifurcation diagrams for no-slip boundary conditions in the basic cell with $L_x = 4\pi/k_c$ and $L_y = 4\pi/\sqrt{3}k_c$. (*a*) Solution branches near the onset of convection. Abbreviations indicate zero Prandtl number with the initial letter Z, otherwise $P = 0.005$. HX denotes perfect hexagons, DHX deformed hexagons. TW identifies travelling waves and R identifies steady rolls. The insets show surface plots of the temperature perturbation θ for the deformed hexagons, the travelling waves and two differently orientated roll states. The travelling wave moves to the left. (*b*) Reduced Nusselt number for travelling rolls (TR) and oblique travelling waves (OTW). The insets show surface temperature plots for the travelling rolls (moving to the left) and the oblique travelling waves (moving to the left and downwards).

free-slip boundary conditions, there is very little change in the integral quantities for this particular solution branch.

The next bifurcation occurs near $Ma = 93$, where the deformed hexagons cease to exist. We have found several solution branches to exist beyond this point. Three of them correspond to stationary two-dimensional rolls either with the roll axes parallel to the short domain boundary or in two different oblique orientations, one of which is shown in the insets in the lower right corner of figure 10(*a*). The other oblique solution is obtained upon reflection with respect to x or y. Notice that there is no difference between the different orientations: the solutions are physically identical. The other two degenerate branches represent time-dependent solutions, namely three-dimensional travelling waves differing only in the direction in which they propagate. These solutions break the spatial reflection symmetry with respect to y. The upper right inset shows such a travelling wave propagating to the left. We have not attempted to resolve the bifurcation scenario in detail since the solutions converge very slowly near $Ma \approx 93$ with integration times of the order of $t_{run} = 100$ or even larger.

The three-dimensional travelling wave solutions are associated with a non-zero mean flow Q_y. For both Prandtl numbers, this mean flow appears to rise from zero for the smallest Ma to a value of approximately $Q_y = 0.25$ for the largest Ma on this solution branch. Figure 10(*a*) also shows that the travelling wave branches exist up to higher Ma than the rolls. Heat transport is slightly more effective for the travelling waves than for straight rolls. Concerning the effect of a finite Prandtl number we note that flow amplitude decreases from $P = 0$ to $P = 0.005$. In comparison with the free-slip case, it is significantly smaller at the same distance from the threshold of convection.

The three-dimensional travelling wave solutions become unstable with respect to purely two-dimensional travelling wave solutions, namely rolls which travel sideways. The roll axes of these solutions are again parallel to the short domain boundary, but in contrast to the three-dimensional travelling waves, the mean flow Q_x is now non-zero, which corresponds to a broken reflection symmetry with respect to x. Previous, purely

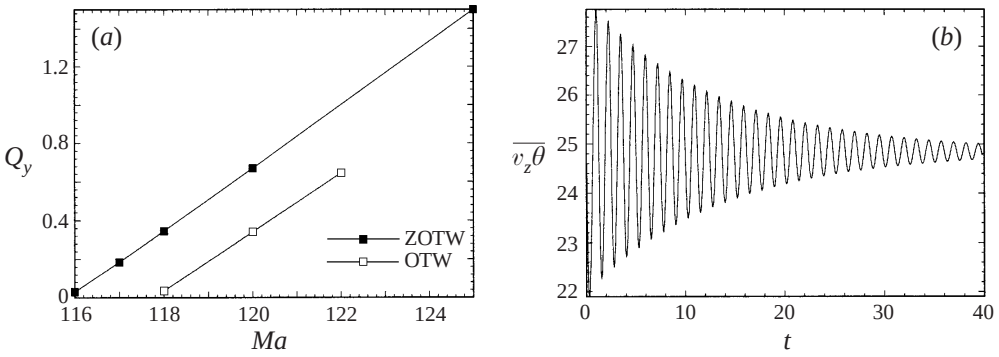

FIGURE 11. (*a*) Dependence of the mass flux Q_y on Ma for the oblique travelling waves in the basic cell for $P = 0$ (ZOTW) and $P = 0.005$ (OTW). (*b*) Temporal evolution of the reduced Nusselt number for $Ma = 118$, $P = 0$.

two-dimensional simulations for $P = 0$ performed in conjunction with Boeck & Thess (1997) demonstrate that the laterally travelling rolls bifurcate from the stationary rolls with $Q_x = 0$. These observations were made for a cell with $L_x = 2\pi/k_c$.

In our present three-dimensional simulations the travelling roll solution sets in only at a somewhat higher Marangoni number than in two dimensions, since the two-dimensional travelling rolls appear to be unstable with respect to the three-dimensional travelling wave solutions for small values of Q_x. This behaviour was observed for $Ma = 108$ with $P = 0$ and for $Ma = 106$ for $P = 0.005$ for rolls parallel to the y-direction. In view of the already considerable complexity of the problem we refrain from tracing the oblique roll solutions any further.

5.2. *Inertial bursts: remnants of flywheel convection*

As for the case of free-slip boundary conditions we shall now describe our findings concerning the regularity of the zero-Prandtl-number limit. We shall again see that inertial convection is not realized, but in contrast to the free-slip condition the flywheel effect represents a noticeable feature of the dynamics.

The two-dimensional travelling roll branches identified by ZTR and TR in figure 10(*b*) exhibit a sharp rise in the flow amplitude over a small range of Marangoni numbers. In two-dimensional simulations with $P = 0$ this strong increase precedes the onset of the flywheel effect, which causes the unbounded growth of the flow amplitude. As for the free-slip boundary condition at the bottom, the regularity of the zero-Prandtl-number limit rests on the prevalence of finite energy solutions beyond the inertial Marangoni number.

In contrast to the free-slip case, the problem of stability of the exponentially growing, two-dimensional solutions arises naturally here since we use the two-dimensional solutions realized just below $Ma_i \approx 116$ as initial conditions for runs with $Ma > Ma_i$. Figure 10(*b*) shows the result of the corresponding numerical experiments. It turns out that the travelling rolls (which exhibit unbounded growth in two dimensions) saturate in a three-dimensional state, in which the basic travelling roll state is still present. These new solutions can be regarded as oblique travelling waves. They are characterized by intense spots of vertical vorticity ω_z along the narrow strips of the free surface where fluid descends into the bulk of the layer. These spots move along the roll axes, giving rise to a mean flow Q_y in addition to Q_x. The strength of Q_y is plotted in figure 11(*a*) for the two cases $P = 0$ and $P = 0.005$. It is rather weak

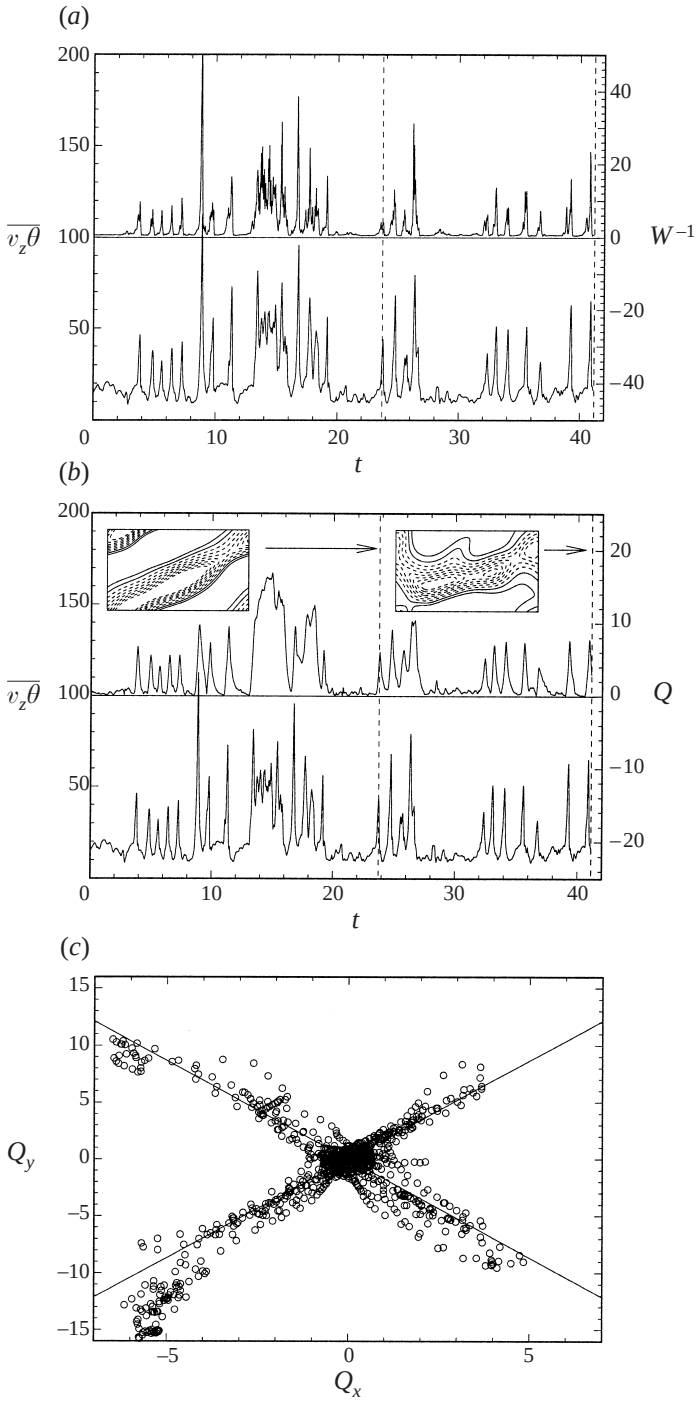

FIGURE 12 (*a–c*). For caption see facing page.

compared with $Q_x \approx 14$. In contrast to the rise of Q_y with Ma, Q_x drops slightly as Ma increases. Notice that $\overline{v_z\theta}$ remains almost constant for the oblique travelling waves. This is also true for other integral quantities. Convergence towards the final state is very slow for these solutions, which is illustrated by figure 11(*b*). Because of

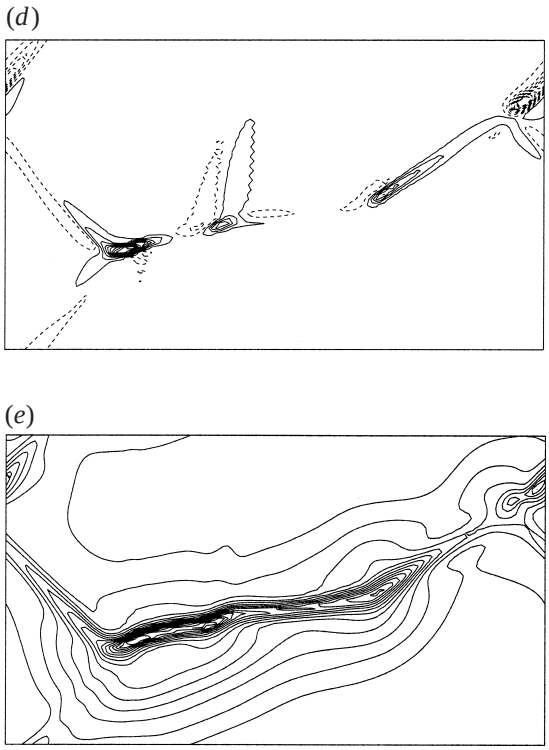

FIGURE 12. Intermittent dynamics for no-slip boundary conditions with $P = 0$, $Ma = 140$ in the basic cell. (*a*) Temporal evolution of the reduced Nusselt number (bottom) and the inverse diagnostic quantity W (top). (*b*) Temporal evolution of $\overline{v_z\theta}$ (bottom) and the mass flux $Q = \sqrt{Q_x^2 + Q_y^2}$ (top). Insets show two surface temperature snapshots taken at the times indicated by the vertical dashed lines, which are identical to those in (*a*). (*c*) Scatter plot from the time series of Q_x and Q_y. (*d*) Surface vorticity snapshot taken at the time corresponding to the right dashed line in (*b*). (*e*) Vertically integrated energy dissipation rate for the same state of the system as in (*d*). Notice the coincidence of locations of high vertical vorticity and high energy dissipation. Contour levels are equidistant in both (*d*) and (*e*).

the exceedingly long integration times, we did not wait for a fully converged solution. The integration was usually stopped at $t \approx 20$. The data given in figures 10(*b*) and 11(*a*) were then obtained by averaging over the last oscillation period.

We have found oblique travelling waves up to $Ma = 125$ for $P = 0$ and $Ma = 122$ for $P = 0.005$. They are replaced by solutions with chaotic time-dependence but with a similar spatial structure. Long transients, also known from RBC at low Prandtl number (Thual 1992), make detailed studies of the transition to chaos very expensive in terms of CPU time. The simulation shown in figure 11(*b*) is fairly typical. At a resolution of $128 \times 32 \times 33$ collocation points in the x-, y- and z-directions and a time step of $\Delta t = 8 \times 10^{-5}$ it required 100 hours user time on four processors of an SGI Origin.

Figure 12(*a*) shows the temporal evolution of the reduced Nusselt number $\overline{v_z\theta}$ for the case $Ma = 140$, $P = 0$ as well as that of W^{-1}. The strongly intermittent character with short, intense bursts is also typical for the finite value $P = 0.005$ at the same Ma. It is apparent from the plots that the bursts coincide with a roll-like flow pattern, i.e. small W. Since two-dimensionalization activates the flywheel effect, the bursts are characterized by exponential growth of the flow amplitude. Breakdown of the

growing solutions is accompanied by a return to a distinctly three-dimensional state. The cause of the breakdown lies in three-dimensional perturbations present in the initial condition at the beginning of the burst. Because of the role of the flywheel effect (leading to inertial convection in two dimensions) during these events we shall refer to them as inertial bursts. We remark that solutions with low W and high heat flux need not necessarily break down immediately but can exist also for longer times as exemplified by the behaviour near $t = 13$. However, judging from our numerical experiments for other Marangoni numbers such behaviour seems to be more of an exception rather than being typical.

The time series of figure 12(b) indicate that the mean flow $Q = \sqrt{Q_x^2 + Q_y^2}$ also grows during the inertial bursts. This agrees with our previous remarks that the flywheel mode is accompanied by a mean flow in the case with no-slip boundary conditions. The insets show surface temperature plots during a burst and after a burst. The oblique orientation of the rolls is actually preferred for the burst events, as can be seen in the scatter plot of figure 12(c). If we decompose the motion of the roll axis of these travelling rolls with oblique orientation with respect to the x- and y-axes (e.g. via observing the surface temperature distribution), we find that $Q_y = \pm\sqrt{3}Q_x$ because of the 60° angle between the roll axis and the y-axis. In figure 12(c) the points with high Q all lie close to the lines $Q_y = \pm\sqrt{3}Q_x$ and not to the Q_x-axis as for rolls parallel to y. As an explanation for this observation we can offer the following argument. If the rolls were parallel to y, then we would actually have two pairs of rolls in our domain. By contrast, this is not the case for the oblique orientation, where only one pair of rolls is actually present. This may account for the preference for the oblique orientation if we assume that the flow settles more easily into the travelling roll state when no synchronization with a second pair of rolls is required.

The resolution of $128 \times 64 \times 33$ collocation points used for the present simulation at $Ma = 140$ may seem rather high when looking at the smooth surface temperature plots in figure 12(b), but the surface vorticity distribution of figure 12(d) shows that it is a necessity. The snapshot was taken at the same time as the surface temperature plot shown in the right inset of figure 12(b). High values of the vertical vorticity occur at the locations with the lowest surface temperature where cold fluid descends into the bulk. These regions also coincide with the highest energy dissipation as can be seen from the vertically averaged energy dissipation rate shown in figure 12(e). We have checked that this is a robust property by repeatedly taking snapshots during the simulation. Moreover, vertical cuts of the vorticity field show that the modulus of $\boldsymbol{\omega}$ is largest at the free surface. The emergence of small structures in the surface vorticity distribution even at moderately supercritical Marangoni numbers suggests that the resolution requirements will be very severe for high-Marangoni-number convection at low Prandtl number. It also highlights the crucial role of the free surface for the flow dynamics. We remark that similar small-scale structures were observed in the simulation with free-slip boundary conditions at $Ma = 120$ and $P = 0$, although this flow was not so strongly intermittent.

In view of this important role of the surface vorticity the numerical resolution was adjusted in such a way that the free-surface vorticity was sufficiently resolved in all of the strongly nonlinear simulations reported here, i.e. it was chosen such that oscillations on the scale of the grid spacing are either absent or of small amplitude (few percent of peak value). Occasional tests with smaller resolution (half the Fourier modes in either one or both horizontal directions) usually yielded deviations in the reduced Nusselt number or the kinetic energy of the order of 1% or less for flows with stationary values of these integral quantities.

6. Discussion and conclusions

We can briefly summarize the numerical simulations reported in the two preceding sections as follows. We have demonstrated that BMC at zero Prandtl number P quickly becomes time-dependent. The same holds true for the finite value $P = 0.005$ approximately equal to that of liquid sodium. In the case of free-slip boundary conditions at the bottom of the layer, the flow is already chaotic when the Marangoni number is about 30% larger than the linear stability threshold for convection. With no-slip conditions, chaotic convection occurs when the Marangoni number is about 60% larger than the threshold. The discrepancy between these two figures may be attributed to the stabilizing effect of bottom friction in the no-slip case. Moreover, the limit of zero Prandtl number is regular, i.e. inertial convection is suppressed in three dimensions. The two-dimensional rolls required for inertial convection are unstable with respect to three-dimensional perturbations when their amplitude is sufficiently large.

All of these results were obtained in a periodic box with aspect ratio $L_x = 4\pi/k_c$, $L_y = 4\pi/\sqrt{3}k_c$. A generalization to larger aspect ratios is of course desirable but hardly feasible on the basis of the present investigations alone. A statement which can probably be made safely is that instabilities will benefit from the presence of more degrees of freedom in larger aspect ratio domains, i.e. more complicated flow patterns may emerge even earlier upon increasing Ma in such domains. We feel that knowledge of the behaviour of the small aspect ratio system should prove useful in investigating these more complicated cases. The considerable numerical effort needed to simulate low-Prandtl-number BMC at only moderately supercritical Ma also favours the use of of a small aspect ratio.

Concerning possible generic properties of our observations (i.e. those unrelated to the constraints imposed by the finite geometry) we note that the transition from hexagonal patterns to stationary rolls for no-slip boundary conditions has been observed by Thess & Bestehorn (1995) at $P \approx 0.2$ for larger aspect ratios also. The canonical approach to determine such generic properties would require analyses similar to those by Busse and co-workers for RBC (e.g. Clever & Busse 1974) rather than direct numerical simulations as done by the present authors. For these analyses one would have to determine the linear stability e.g. of the infinitely extended hexagonal pattern with respect to perturbations of suitable symmetry as function of the Marangoni number, the basic wavelength and other parameters. To the knowledge of the authors this has so far not been attempted in BMC.

The question of how RBC and BMC compare for low Prandtl number can be addressed in a more substantial way. A major difference between RBC and BMC consists in the different planform at the onset of convection, namely rolls for RBC and hexagons for BMC. Consequently, one cannot expect similar behaviour concerning the route to chaos. In addition, direct comparison with Thual's (1992) results is difficult because the cells considered there were typically at least 50% smaller. If we had chosen these smaller aspect ratios, the perfect hexagonal pattern would not have occurred at all. However, our observations share some similarities with his findings concerning the differences between free-slip and no-slip boundary conditions at the bottom. A typical difference appears to be the generation of oscillatory states in the free-slip case, whereas travelling waves appear for no-slip conditions. This may be related to the additional constraints of the conserved linear momentum for the free-slip bottom.

Another similarity consists in the strong intermittency of the flow for zero Prandtl

number with a no-slip bottom when the applied temperature gradient exceeds the threshold for inertial convection. For both RBC and BMC the flow apparently has the tendency to evolve into a nearly two-dimensional state which activates the flywheel effect and causes exponential growth, cf. § 5.3 in Thual (1992). The breakdown of this growing solution is caused by the generation of vertical vorticity. We remark that the evolution towards the two-dimensional roll pattern in our BMC simulations generates a significant mean flow. The simplest way of assessing its role could be to set the two mean flow components U and V equal to zero in future simulations.

Strongly intermittent behaviour at zero Prandtl number is also reported in RBC for free-slip conditions immediately above the threshold of convection. In a small square cell which admits a single pair of rolls Thual (1992) observes relaxation oscillations where the rolls change their orientation periodically in the cell. The change is mediated by the generation of vertical vorticity, which apparently requires a considerable flow amplitude. Curiously, Thual does not refer to the flywheel effect in connection with this observation, although the threshold for inertial convection coincides with the linear stability threshold for RBC between free-slip plates. In our simulations of BMC, the larger aspect ratio does not favour a two-dimensional organization so strongly, and the flow remains in a three-dimensional state, which suppresses the strong intermittency caused by the flywheel effect.

An interesting open problem concerns the stability of the exponentially growing roll solutions. It would be interesting to determine which perturbations eventually give rise to the breakdown of the two-dimensional state. Since the underlying basic state is time-dependent this poses a problem which cannot simply be addressed in the framework of standard hydrodynamic stability, i.e. straightforward linearization or Floquet theory. Future investigations should also look into the effects of a magnetic field, which should be able to stabilize two-dimensional rolls when it is oriented parallel to the roll axis. For RBC, there are works dealing with such questions (Meneguzzi *et al.* 1987; Sulem, Sulem & Thual 1985).

Although experimental work on BMC in liquid metals requires considerable effort, we hope that the present results can convince experimentalists that this problem is worth studying. Current efforts of the authors are directed towards further increases in the Marangoni number in order to obtain a numerical realization of turbulent BMC.

We are grateful to our colleagues in Dresden, specifically to K. Eckert, R. Schaller and O. Zikanov, and to F. Busse, A. Pumir, A. Nepomnyashchy and I. Simanovskii for interesting discussions. We also wish to thank the referees for their substantial suggestions for improvement of the paper. Computer resources were provided by the Computing Centers at the Research Center Jülich (HLRZ) and at the Universities of Dresden and Ilmenau. T. B. is supported by the Deutsche Forschungsgemeinschaft under grants Th497/9-2 and Th497/9-3.

REFERENCES

Bestehorn, M. 1993 Phase and amplitude instabilities for Bénard–Marangoni convection in fluid layers with large aspect ratio. *Phys. Rev.* E **48**, 3622–3634.

Boeck, T. & Thess, A. 1997 Inertial Bénard–Marangoni convection *J. Fluid Mech.* **350**, 149–175.

Boeck, T. & Thess, A. 1998 Turbulent Bénard–Marangoni convection: Results of two-dimensional simulations. *Phys. Rev. Lett.* **80**, 1216–1219.

Busse, F. H. & Clever, R. M. 1981 An asymptotic model of two-dimensional convection in the limit of low Prandtl number. *J. Fluid Mech.* **102**, 75–83.

Canuto, C., Hussaini, M. Y., Quarteroni, A. & Zang, T. 1988 *Spectral Methods in Fluid Dynamics*. Springer.

Carpenter, B. M. & Homsy, G. M. 1990 High Marangoni number convection in a square cavity: Part II. *Phys. Fluids* A **2**, 137–149.

Chandrasekhar, S. 1961 *Hydrodynamic and Hydromagnetic Stability*. Oxford University Press.

Chiffaudel, A., Fauve, S. & Perrin, B. 1987 Viscous and inertial convection at low Prandtl number: Experimental study. *Europhys. Lett*. **4**, 555–560.

Clever, R. M. & Busse, F. H. 1974 Transition to time-dependent convection. *J. Fluid Mech.* **65**, 625–645.

Clever, R. M. & Busse, F. H. 1990 Convection at very low Prandtl numbers. *Phys. Fluids* A **2**, 334–339.

Dauby, P. C., Lebon, G., Colinet, P. & Legros, J. C. 1993 Hexagonal Marangoni convection in a rectangular box with slippery walls. *Q. J. Mech. Appl. Maths* **46**, 683–707.

Davis, S. H. 1987 Thermocapillary instabilities. *Ann. Rev. Fluid Mech.* **19**, 403–435.

Eckert, K., Bestehorn, M. & Thess, A. 1998 Square cells in surface-tension-driven Bénard convection: experiment and theory. *J. Fluid Mech.* **358**, 149–197.

Ginde, R. M., Gill, W. N. & Verhoeven, J. D. 1989 An experimental study of Rayleigh–Bénard convection in liquid tin. *Chem. Engng Commun.* **82**, 223–228.

Gollub, J. P. & McCarriar, A. R. 1982 Convection patterns in Fourier space. *Phys. Rev.* A **26**, 3470–3476.

Golovin, A. A., Nepomnyashchy, A. A. & Pismen, L. M. 1997 Nonlinear evolution and secondary instabilities of Marangoni convection in a liquid-gas system with deformable interface. *J. Fluid Mech.* **341**, 317–341.

Gottlieb, D. & Orszag, S. A. 1977 *Numerical Analysis of Spectral Methods*. CBMS–NSF Regional Conference Series in Applied Mathematics, Philadelphia.

Jackson, E., She, Z.-S. & Orszag, S. A. 1991 A case study in parallel computing: I. Homogeneous turbulence on a hypercube. *J. Sci. Comput*. **6**, 27–45.

Kuhlmann, H. C. & Rath, H. J. 1993 Hydrodynamic instabilities in cylindrical thermocapillary liquid bridges. *J. Fluid Mech.* **247**, 247–274.

Landau, L. D & Lifshitz, E. M. 1987 *Fluid Mechanics*. Course of Theoretical Physics, vol. 6. Pergamon Press.

Levenstam, M. & Amberg, G. 1995 Hydrodynamical instabilities of thermocapillary flow in a half-zone. *J. Fluid Mech.* **297**, 357–372.

Matthews, P. C. 1998 Hexagonal patterns in finite domains. *Physica* D **116**, 81–94.

Meneguzzi, M., Sulem, C., Sulem, P. L. & Thual, O. 1987 Three-dimensional numerical simulation of convection in low Prandtl number fluid. *J. Fluid Mech.* **182**, 169–191.

Pearson, J. R. A. 1958 On convection cells induced by surface tension. *J. Fluid Mech.* **4**, 489–500.

Proctor, M. R. E. 1977 Inertial convection at low Prandtl number. *J. Fluid Mech.* **82**, 97–114.

Pumir, A. & Blumenfeld, L. 1996 Heat transport in a liquid layer locally heated on its free surface. *Phys. Rev.* E **54**, R4528–R4531.

Schiller, S., Heisig, U. & Panzer, S. 1982 *Electron Beam Technology*. Wiley.

Sulem, P., Sulem, C. & Thual, O. 1985 Direct numerical simulation of three-dimensional convection in liquid metals. *Prog. Astron. Aeronaut*. **100**, 125–151.

Thess, A. & Bestehorn, M. 1995 Planform selection in Bénard–Marangoni convection: l hexagons versus g hexagons. *Phys. Rev*. **52**, 6358–6367.

Thess, A. & Orszag, S. A. 1995 Surface-tension-driven Bénard convection at infinite Prandtl number. *J. Fluid. Mech.* **283**, 201–230.

Thual, O. 1992 Zero-Prandtl-number convection. *J. Fluid Mech.* **240**, 229–258.

VanHook, S. J., Schatz, M. F., Swift, J. B., McCormick, W. D. & Swinney, H. L. 1997 Long-wavelength surface-tension-driven Bénard convection: experiment and theory. *J. Fluid Mech.* **345**, 45–78.

Zebib, A., Homsy, G. M. & Meiburg, E. 1985 High Marangoni number convection in a square cavity. *Phys. Fluids* **28**, 3467–3476.